Energy Storage Materials 8 (2017) 209–216

Contents lists available at ScienceDirect

Energy Storage Materials

journal homepage: www.elsevier.com/locate/ensm

Nanosized Li_2S-based cathodes derived from MoS_2 for high-energy density Li–S cells and Si–Li_2S full cells in carbonate-based electrolyte

Juan Balach[a,b,*], Tony Jaumann[b], Lars Giebeler[b]

[a] Department of Chemistry, Universidad Nacional de Río Cuarto-CONICET, Route 36 Km 601, X5804ZAB Río Cuarto, Argentina
[b] Leibniz Institute for Solid State and Materials Research (IFW) Dresden e.V., Helmholtzstraße 20, D-01171 Dresden, Germany

ARTICLE INFO

Keywords:
MoS_2 electrode
Li_2S cathode
Carbonate-based electrolyte
High areal capacity
Lithium-sulfur battery
Full cell

ABSTRACT

Conversion-type lithium-sulfur (Li–S) batteries tend to become the follow-up system for classical Li-ion batteries based on the intercalation principle. However, the practical application of rechargeable Li–S batteries is still counteracted by fast capacity fading and poor cycling stability caused by the major obstacle of these systems: the polysulfide shuttling. Herein, a feasible *in cell* formation of nanosized Li_2S *via* full lithiation and irreversible decomposition of MoS_2 nanoparticles is proposed. The primary advantage of the resulting Mo/Li_2S-based cathode is found in the absence of soluble polysulfide species, allowing its operation in carbonate-based electrolytes. By adjusting the operating condition, Li–S cells in carbonate-based electrolyte with an ultrahigh Li_2S loading of 10.7 mg cm^{-1} demonstrate good cycle stability and a high average areal capacity of 7.5 mA h cm^{-2}. In order to tackle uncontrollable lithium dendrite formation, our simple-prepared cathode was successfully coupled with a nanostructured silicon anode to fabricate a Li–S full-cell capable to provide a high capacity of ≈780 mA h g^{-1}, based on the sulfur mass. This easy and effective approach for preparing high-load Li_2S cathodes will advance progress in the development of sulfur-based battery technology.

1. Introduction

Advanced progress on transport electrification—hybrid/electric vehicles and aerospace industry—or for smart-grid applications can only be burst it in tandem with the development of new high-energy rechargeable battery technologies which are able to go far beyond the energy densities of traditional lithium-ion batteries (LIBs). LIBs have achieved an overwhelming successful on portable electronic devices. However, today's commercial LIBs manufactured with lithium transition metal oxide cathodes cannot satisfy the upcoming energy-market requirements due to their restricted specific energy densities—up to 400 W h kg^{-1} —and still critical safety concerns [1,2]. Considering its high theoretical specific energy density of 2600 W h kg^{-1}, the lithium–sulfur (Li–S) battery system is heading as the most suitable choice to fulfill future energy demands [3], especially after upcoming and most probably successful introduction into the commercial market by companies, e.g. Oxis Energy.

However, the practical production of Li–S batteries is dogged by inherent challenges to reach the maximum performance possibility, e.g. expected specific energies of 400 W h kg^{-1} in 2017 and 500 W h kg^{-1} in 2019 by Oxis Energy company [4]. A large variety of well-designed sulfur-infiltrated porous hosts and lithium sulfide (Li_2S)-carbon composite cathodes have proven to overcome the general issue of a poor conductivity of sulfur/lithium sulfide and their large volume changes during de-/lithiation [5–10]. Some of these approaches are even too expensive when thought on an industrial scale. Nevertheless, the possible dissolution of polysulfide redox intermediates and their further shuttling is the key drawback that needs to be overcome to realize the commercialization of this technology. The shuttle effect involves the migration of dissolved polysulfide intermediates between the cathode and the anode by simple polysulfide concentration gradient forces. This phenomenon induces the passivation of the anode surface by redeposition of polysulfide discharging products and the corrosion of the lithium metal anode, causing an active material loss, fast capacity fading and poor cycling stability [11]. To circumvent this hurdle, the reconfiguration of the cell design by using carbon interlayers or functional hybrid separators and the development of novel ether-based electrolytes with polysulfide-sorbent additives have been implemented to retain the dissolved polysulfide compounds at the cathode site during cycling [12–17]. Despite the resulting improvement of cyclability and cell performance, these approaches still cannot completely suppress the shuttle phenomenon and further loss of active material. To cope with the challenging polysulfide shuttle issue, a new and versatile strategy must be adopted.

* Corresponding author at: Department of Chemistry, Universidad Nacional de Río Cuarto-CONICET, Route 36 Km 601, X5804ZAB Río Cuarto, Argentina.
E-mail address: jbalach@exa.unrc.edu.ar (J. Balach).

http://dx.doi.org/10.1016/j.ensm.2017.03.013
Received 10 January 2017; Received in revised form 9 March 2017; Accepted 19 March 2017
Available online 24 May 2017

Among other transition metal dichalcogenides, molybdenum disulfide (MoS_2) has been widely investigated as a potential anode candidate for lithium-ion batteries due to the high delivered capacity when it is fully discharged (lithiation process) down to low voltages (i.e: 0.01 V *vs.* Li/Li^+) and thus enabling the coupling with a high-voltage lithium metaloxide (LMO) cathode [18]. Earlier research works reported that MoS_2 reversibly reacts with 4 mol of Li to form metallic Mo and Li_2S ($MoS_2 + 4Li \leftrightarrow 4Mo + 2Li_2S$). However, theoretical studies [19] and experimental analyses [20–22] recently demonstrated that after the first cycle with an initial discharge step of 0.01–0.02 V *vs.* Li/Li^+, the chemical reaction predominantly proceeds between Li and S rather than MoS_2 and Li. This observation means that the reaction mechanism of the cell becomes a kind of a Li–S battery system. Interestingly, the *in-situ* preparation of Li_2S-based electrodes derived from MoS_2 (or MoS_2/carbon composites) as starting material has rarely been explored for Li–S battery systems [20,21].

In this contribution, we demonstrate a feasible and simple methodology to improve the electrochemical stability of high-load sulfur-based cathodes in a carbonate-based electrolyte by taking the advantage of the MoS_2 chemistry and the particle size effect of the MoS_2 to form nanosized Li_2S *in-situ* at cell level. To proof this concept, a simple mixture of commercially available components (MoS_2 nanoparticles, conductive carbon and polymeric binder) was used to prepare the elementary cathode electrode. After full lithiation of the MoS_2, Li_2S nanoparticles are produced into a highly stable polymeric gel-like film (derived from the electrolyte decomposition) which tightly confines sulfur-based species into it. As a result of the unique features of the Mo/Li_2S-based cathode, Li–S cells in carbonate-based electrolyte with ultrahigh Li_2S loadings (up to 10.7 mg cm^{-1}) exhibit good cycle stability and a high average areal capacity of 7.5 mA h cm^{-2}, one of the highest reported so far for MoS_2- or Li_2S-based cathodes. Furthermore, our simple cathode was successfully coupled with a nanostructured silicon anode to fabricate a Li-ion full-cell able to deliver a high capacity of ≈780 mA h g^{-1} based on the sulfur mass. On this basis, we believe that this study provides an effective approach to avoid polysulfide formation and to fabricate high-loading and stable sulfur-based cathodes for post lithium-ion battery systems.

2. Experimental section

2.1. Preparation of elementary Li_2S-based cathode preparation

As the simplest design of the Li_2S-based cathode, a slurry of commercially available MoS_2 nanoparticles (Sigma-Aldrich, 99 wt%, 90 nm) (80 wt%), Super P Li (Timcal) (10 wt%) and acacia-derived gum arabic binder (Sigma-Aldrich) (10 wt%) was prepared in deionized water by shaker-milling for 30 min. The homogeneous slurry was blade casted onto Cu foil (MTI Corp., 10 μm thickness). The cathodes were dried at 100 °C for 20 h and then punched into circular disks of 12 mm in diameter. The initial MoS_2 loading of the electrode is 5.0–7.5 mg cm^{-2}. Considering full decomposition of MoS_2 after lithiation, the final Mo/Li_2S cathode has a Li_2S loading of around 2.0–3.0 mg cm^{-2} and a Li_2S content of 40 wt%. In order to evaluate the cell performance at ultrahigh areal Li_2S loading, a slurry consisting of MoS_2 nanoparticles (80 wt%), Super P Li (10 wt%) and polyacrylic acid (Sigma-Aldrich, Mv ≈ 450,000) (10 wt%) was prepared in ethanol by shaker-milling for 30 min and then the slurry was drop-coated on a copper foam with a diameter size of 12 mm. Finally, the high-loading cathode with 10.7 mg_{Li2S} cm^{-2} was obtained after drying at 100 °C for 20 h.

2.2. Electrochemical measurements

Coin cells (CR2025) were assembled in an Ar-filled glove box. Glass fiber layers (Whatman) were used as separator and lithium metal foil (Chempur, 250 μm thick, 13 mm diameter) was used as counter electrode. The electrolyte consisted of 1 M $LiPF_6$ in ethylene carbonate (EC)/dimethyl carbonate (DMC) (1:1 v/v) (LP30 Selectilyte, BASF).

Half-cells were galvanostatically cycled in the range of 0.01–3.0 V *vs.* Li/Li^+ at 25 °C using a BaSyTec Cell Test System (CTS). Cyclic voltammograms (CV) and electrochemical impedance spectroscopy (EIS) analysis were conducted using a VMP3 potentiostat (Bio-logic). EISs measurements were performed between 300 kHz and 10 mHz using an AC voltage amplitude of 10 mV at 3.0 V closed to the open-circuit voltage. Prior to the cycling performance tests, the cells were cycled between 0.01–3.0 V *vs.* Li/Li^+ at a current rate of 117 mA g^{-1} for the first cycle as preconditioning step to form the active Li_2S material and thus activate the electrode for Li–S cells. The calculation of specific discharge capacities is based on the mass of Li_2S (1 C = 1166 mA g^{-1}) and based on the equivalent mass of sulfur (1 C = 1675 mA g^{-1}).

For full-cell tests, 10% v/v of fluoroethylene carbonate (FEC, Sigma-Aldrich, > 99.9%) was added to the LP30 electrolyte in order to stabilize the Si anode [23,24]. A nanostructured silicon/carbon composite (Si@C) was used as anode electrode. The synthesis of the Si@C is described in our previous report [24]. Prior to full-cell assembling, the silicon anode was assembled *versus* lithium metal with LP30 + 10% v/v FEC electrolyte in Swagelok cells and discharged to 10 mV at 0.5 mA cm^{-2}. The silicon anode was about 20% over dimensioned in terms of capacity with a total electrode weight of 3.9 mg cm^{-2} (before lithiation). Finally, the lithiated silicon anode was assembled *versus* the MoS_2 cathode in Swagelok cell configuration. Following common literature conventions, discharging and charging of both half-cells and full-cells are defined as the lithiation and delithiation processes, respectively, regarding the MoS_2 cathode.

2.3. Characterization

The morphology of the MoS_2 nanoparticles and the cycled electrodes were investigated by using a Zeiss Leo Gemini 1530 scanning electron microscope (SEM). Transmission electron microscopy (TEM) imaging was performed with a FEI Tecnai F30 equipped with a field emission gun (FEG) working at 300 kV. The SAED patterns were analyzed with the in-house program ELDISCA [25]. X-ray power diffraction (XRD) experiments were achieved in transmission geometry with Cu $K_{\alpha 1}$ radiation on an STOE Stadi P diffractometer with a curved Ge(111) crystal monochromator and a 6°-position sensitive detector. For Rietveld analysis the program MAUD was used [26]. The Popa line broadening model was used to determine crystallite sizes and strain. Due to strong texture of the crystalline MoS_2 [27] and $LiMoS_2$ [28] phases, a harmonic texture model with 2/*mmm* symmetry was applied. For Li_2S a structure model with space group $Fm\bar{3}m$ was used [29]. Pristine Mo (Sigma-Aldrich, 99 wt%), Li_2S (Sigma-Aldrich, 99.98 wt%) and MoS_2 samples which are stable in air, were prepared as thin films on an acetate foil fixed with a collodion glue and were recorded in a 2θ range from 10° to 80° with a step size of Δ2θ = 0.02°. For *post-mortem* investigation, the cells were cycled at a current rate of 117 mA g^{-1} between 0.01–3.0 V *vs.* Li/Li^+ and disassembled at different de-/lithiated states inside a glove box under argon atmosphere. Then the samples were washed three times with DMC (BASF Selectilyte) and dried under vacuum at room temperature. The samples prepared for XRD analysis were pressed between Kapton tapes under argon atmosphere to avoid contact with air during measurement. The samples transferred into the SEM, were exposed to air for about 2 min.

3. Results and discussion

3.1. Structural and morphology characterization

Commercially available MoS_2 nanoparticles were used as starting material to prepare nanosized Li_2S by the electrochemical decomposition reaction of MoS_2 at low potential (Scheme 1). In general, the

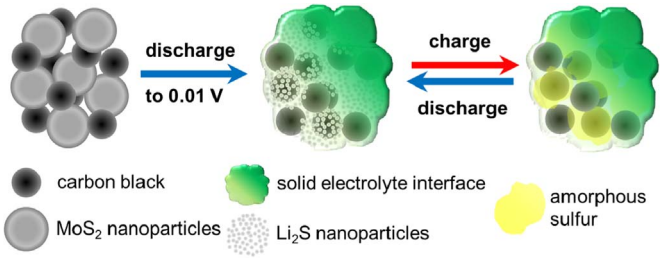

Scheme 1. Simplified illustration of the *in cell* formation of Li_2S nanoparticles *via* full lithiation and irreversible decomposition of MoS_2 nanoparticles.

lithiation mechanism of MoS_2 during the initial discharge reaction can be divided into two steps: (i) intercalation of lithium into MoS_2 in the voltage range of 3.0–1.0 V *vs.* Li/Li^+ as shown in Eq. (1), and (ii) irreversible decomposition reaction of MoS_2 to Li_2S and metallic Mo at approximately 0.6 V *vs.* Li/Li^+ as described by Eq. (2). Note that within the voltage range of reaction (1), the lithiation/delithiation process is fully reversible and the theoretical specific capacity of this reaction is 167 mA h g^{-1} [20], while the full discharge process—Eqs. (1) and (2)—has a theoretical specific capacity is 669 mA h g^{-1} [18]. Upon full decomposition of MoS_2 to Li_2S and Mo at 0.01 V *vs.* Li/Li^+, the subsequent charge/discharge cycles are ruled by the Eq. (3). The reactions should not be taken as sudden but more in the sense of a gradient starting and finalizing at certain potentials and a transition from one reaction step to the other.

$$MoS_2 + xLi^+ + xe^- \leftrightarrow Li_xMoS_2\ (0.6\ V \le U < 1.2\ V\ vs.\ Li/Li^+) \quad (1)$$

$$Li_xMoS_2 + (4-x)Li^+ + (4-x)e^- \rightarrow Mo + 2Li_2S\ (0.01\ V \le U < 0.6\ V\ vs.\ Li/Li^+) \quad (2)$$

$$Mo + 2Li_2S \leftrightarrow Mo + 2S + 4Li\ (\approx 2.3\ V\ vs.\ Li/Li^+) \quad (3)$$

To investigate the structural changes of the MoS_2-based cathode, *ex-situ* XRD analyses were conducted at different depths of discharge and state of charge as shown in Figs. 1 and S1. The fresh cathode shows the characteristic reflections corresponding to pristine MoS_2 nanoparticles (Fig. 1a) with a hexagonal crystal structure ($P6_3/mmc$). The crystallite size of MoS_2 was determined to be 86 nm. When discharged to 1.2 V *vs.* Li/Li^+, the reflections are a bit broader due to shrinkage of crystallites, but still remain in the distinctive position of MoS_2 (Fig. S1). As the discharge process continues to 0.6 *vs.* Li/Li^+, the reflections positioned at higher angle associated with MoS_2 became much broader and shifted to slightly lower angles, indicating a structure modification of MoS_2 to $LiMoS_2$-type like structure (Fig. 1b). This observation is explained by the expansion through the *d*-spacing of the MoS_2 structure due to the intercalation of Li^+ ions, as suggested by Eq. (1) [18]. The expansion causes a distortion of the entire hexagonal crystal system and transforms the crystal structure to the lowest triclinic symmetry (space group *P*-1). Once the cell is fully discharged to 0.01 V *vs.* Li/Li^+ (Fig. 1c), the representative reflections of MoS_2 completely vanish, while few characteristic reflections of Li_2S (at 27.0°, 30.9° and 45.0°) as well as a broad reflection at ≈40° appear, typical for metallic Mo [30], which corresponds to the reaction mechanism expressed in Eq. (2). By applying the Scherrer equation, the crystallite sizes of Li_2S and Mo were calculated to be 15 and 0.8 nm, respectively. Interestingly, after recharging the electrode to 3.0 V *vs.* Li/Li^+, a diffraction pattern without obvious reflections is recorded (Fig. S1), indicating that the formed products are amorphous (probably sulfur and molybdenum) [20]. This behavior demonstrates that the MoS_2 discharged at low voltage (i.e. 0.01 V *vs.* Li/Li^+) easily decomposes to an active Li_2S material.

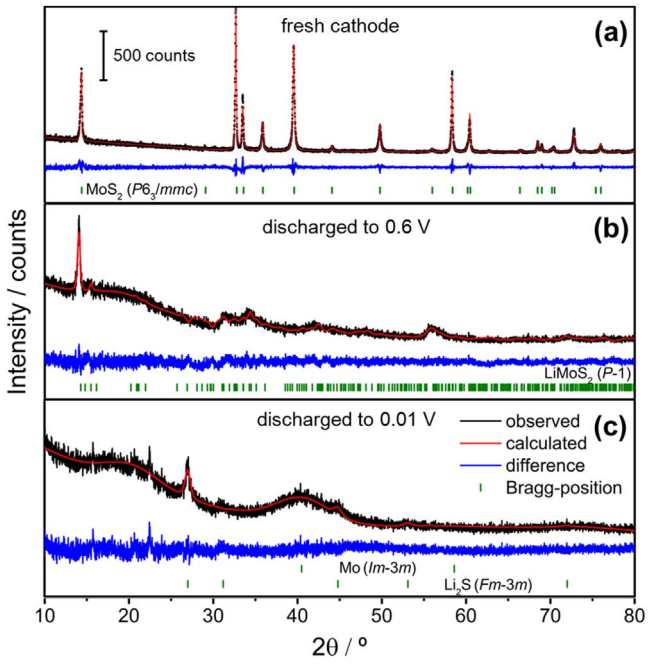

Fig. 1. Observed and calculated XRD pattern of (a) fresh cathode, (b) cathode discharged to 0.6 V *vs.* Li/Li^+ and (c) cathode discharged to 0.01 V *vs.* Li/Li^+.

The morphology of the initial MoS_2 electrode and its changes at discharge and charge stages were investigated by SEM and TEM. Fig. 2a and b show the representative part of MoS_2 nanoparticles consisting of crystallites with an average size of 52 nm (40–110 nm). Furthermore, the diffraction spots in the SAED pattern of Fig. 2c form a ring pattern which indexing well with large (overlapping) crystalline domains in the MoS_2 nanoparticles of the fresh electrode (space group $P6_3/mmc$ [27]). The SEM image of the fully discharged electrode at 0.01 V *vs.* Li/Li^+ (Fig. 2d) shows the formation of agglomerated particles with an average size of 123 nm (75–176 nm). These particles are covered by the so-called solid electrolyte interface (SEI) layer, which is a typical surface film formed in lithium-ion batteries by the electrolyte decomposition during the discharge process (≈0.6 *vs.* Li/Li^+) [24,31]. The increase in size of the grain particles can be explained by both the insertion of Li^+ ions which swells the volume of the discharged products and the additional polymeric layer associated with the SEI formation. The TEM image in Fig. 2e displays 10–15 nm dark spots (orange circles) and numerous small gray dots with a particle size of ≈1.5 nm (indicated by orange arrows) uniformly distributed through the SEI film (marked by white arrows). The ring pattern in the SAED image further reveals the presence of nanocrystalline Li_2S (space group $Fm\bar{3}m$ [29]) (Fig. 2f), confirming the formation of the desired active Li_2S material at the end of the discharging process, following Eq. (2). When the electrode is recharged to 3.0 V *vs.* Li/Li^+, the average size of the grain particles decreased from 123 nm to 82 nm (49–132 nm) (Fig. 2g), which is attributed to the delithiation process. In concordance with the XRD investigation presented above (Fig. S1), the TEM image in Fig. 2h further confirms the absence of crystalline structures since no lattice fringes are visible, indicating that the products of charging are amorphous.

3.2. Electrochemical performance (half-cell)

To get more information about the formation of Li_2S and its potential use as active cathode material for Li–S cells, galvanostatic discharging/charging voltage profiles and cyclic voltammetry tests were performed. Fig. 3a shows the discharging/charging curves corresponding to the initial and second cycle at 0.1 C (1 C = 1166 mA g^{-1}) for the half-cells with MoS_2 nanoparticles as starting cathode material. During the initial discharging (lithiation) process, the cell shows two main reductions plateaus at ≈1.1 and ≈0.6 V *vs.* Li/Li^+ corresponding to the characteristic two-step MoS_2 reduction reactions [18]. The discharge

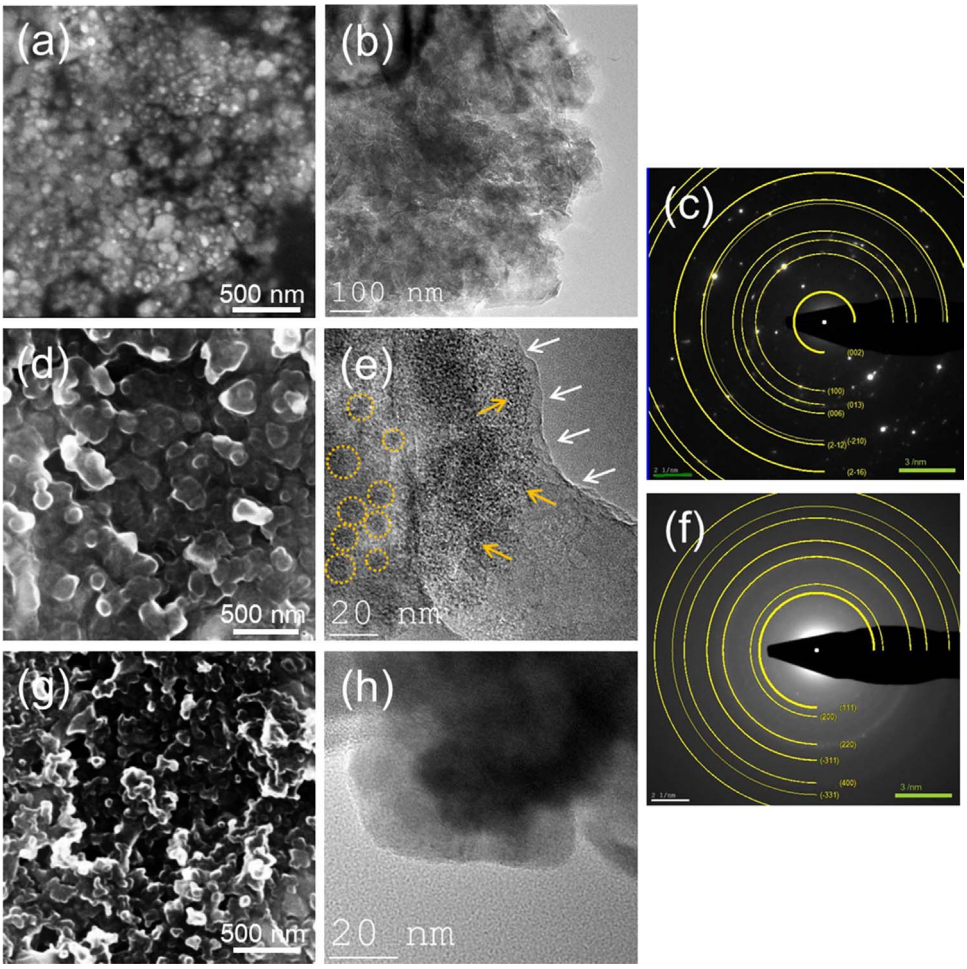

Fig. 2. a) SEM image, b) TEM image and c) the corresponding SAED pattern of the initial MoS_2-based cathode with simulation (yellow) of the MoS_2 structure ($P6_3/mmc$). d) SEM image, e) TEM image and f) the corresponding SAED pattern of the discharged cathode with simulation (yellow) of the Li_2S structure ($Fm\bar{3}m$). g) SEM image and h) TEM image of the recharged cathode. (For interpretation of the references to color in this figure legend, the reader is referred to the web version of this article.)

plateau at higher potential is related to the intercalation of Li^+ ions into MoS_2 accompanied by a structure transformation (Eq. (1)) and the discharge plateau at lower potential is assigned to the further irreversible conversion reaction of Li_xMoS_2 to Li_2S and Mo (Eq. (2)). It is also worth mentioning that the SEI film is usually formed at potentials below 0.8 V *vs.* Li/Li^+ as a result of electrolyte decomposition [32]. In the charging (delithiation) process, only one charge plateau at ≈2.2 V *vs.* Li/Li^+ is identified. This charge plateau is attributed to the reversible oxidation reaction of Li_2S to sulfur, according to Eq. (3). In the second discharging process, the voltage profile shows a complete different behavior with three discharge plateaus at ≈2.0, 1.2 and 0.4 V *vs.* Li/Li^+ instead of the initial two plateaus, indicating a differing lithiation mechanism. The plateau at ≈2.0 *vs.* Li/Li^+ is assigned to the reductive conversion of sulfur to Li_2S, while the following plateau at ≈1.2 *vs.* Li/Li^+ is ascribed to the association of Li with Mo [20,33,34]. The plateau below 0.5 *vs.* Li/Li^+ could correspond to that Li binding on the defect sites of hard carbons (i.e. black carbon, porous carbon) and on basal plane of nanostructured carbons (i.e. graphene). Normally, the intensity of this plateau is gradually diminishing upon cycling [18].

Cyclic voltammetry studies performed between 0.01 and 3.0 V *vs.* Li/Li^+ at 0.05 mV s^{-1} further evidences the successful formation of Li_2S (Fig. 3b). The first and second CV curves exhibit cathodic and anodic peaks at similar potentials consistent with those obtained from the initial discharging/charging voltage profiles discussed above (Fig. 3a). Generally, Li–S half-cells operated in carbonate-based electrolyte present a sudden capacity fading after the first cycle due to side reactions between polysulfide species and carbonate-based compounds by nucleophilic addition or substitution reaction [35]. However, the unique features of our sulfur-based cathode with Li_2S nanoparticles produced *in-situ* are embedded into a highly stable polymeric gel-like SEI film demonstrating a high stability in a carbonate-based electrolyte system due to the lack of soluble polysulfides formation. It is worth pointing out that the cycling of the MoS_2 electrode between 0.8 and 3.0 V *vs.* Li/Li^+ (Fig. S2) displays a completely different lithium storage mechanism in comparison with the voltammograms shown in Fig. 3b. Without the previous deep discharge step to 0.01 V *vs.* Li/Li^+, the mechanism of the reaction is principally directed by the reversible intercalation of Li^+ ions into MoS_2 to form Li_xMoS_2 (Eq. (1)) [21]. These results demonstrate that after the first cycle between 0.01 and 3.0 V *vs.* Li/Li^+ (henceforth denoted as activation cycle), the reaction is mainly between Li and S rather than Li and MoS_2, leading to the fact that the *in-situ* formation of Li_2S nanoparticles can be easily controlled by keeping in mind the redox chemistry of the MoS_2 when it is coupled with Li.

Numerous publications on LIBs with MoS_2-based electrodes have reported higher experimental specific capacities than the expected theoretical specific capacity of MoS_2 (669 mA h g^{-1}). This peculiarity is generally explained by the additional Li intercalation on defect sites of MoS_2 [18] and the intrinsic charge storage capacities of carbon nanostructures used as support material and/or conductive additives [36–39]—their contribution are generally neglected in the calculations. Additionally, the calculation of the capacity is usually related to the

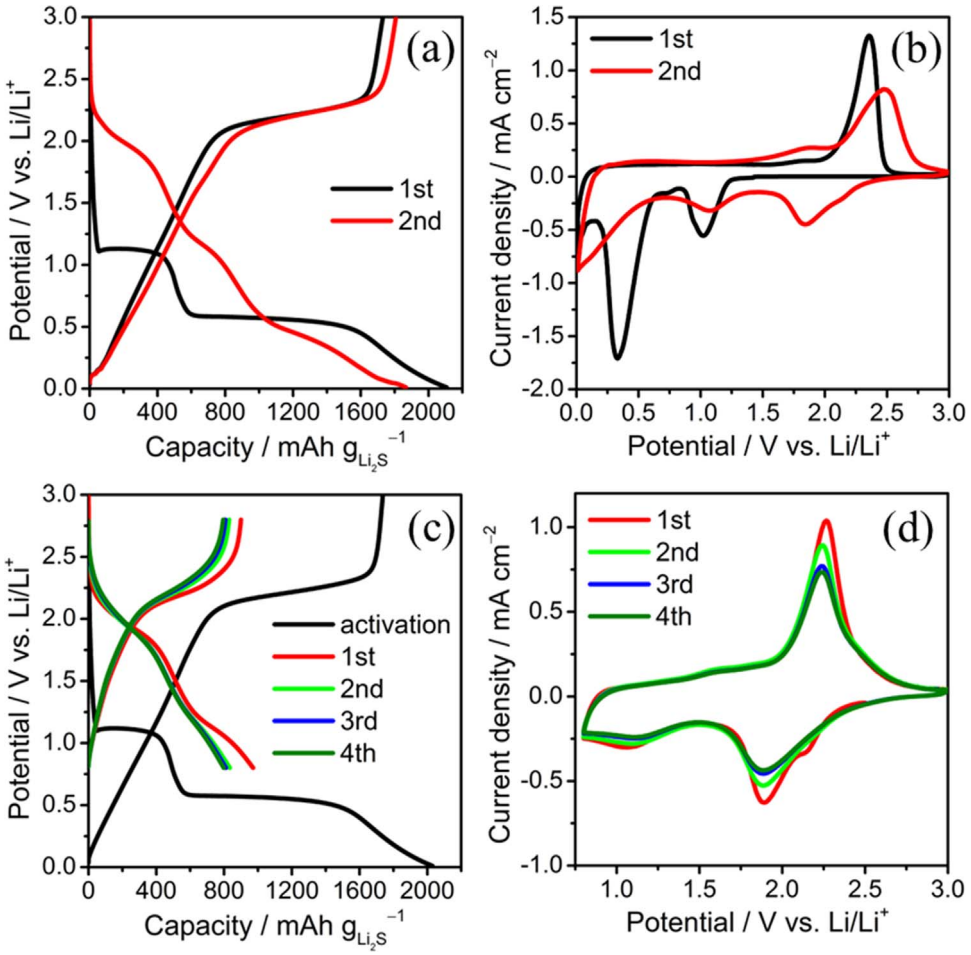

Fig. 3. (a) Galvanostatic dis-/charging voltage profile (C-rate = 0.1, 0.01 V ≤ *U* ≤ 3 V *vs.* Li/Li^+) and (b) cyclic voltammograms (scan rate: 0.05 mV s^{-1}) of the half-cells with MoS_2 nanoparticles as starting cathode material within a potential window of 0.01–3.0 V *vs.* Li/Li^+. (c) Galvanostatic dis-/charging voltage profile (C-rate of 0.1) and (d) cyclic voltammograms (scan rate: 0.05 mV s^{-1}) of the half-cells with MoS_2 nanoparticles as starting cathode material after activation cycle and application of reduced potential window of 0.8–3.0 V *vs.* Li/Li^+.

MoS_2 instead of the formed active Li_2S material.

Considering the high discharging capacity delivered by the Li–S half-cell (around 1800 mA h g^{-1} based on Li_2S, Fig. 3a), the proposed approach to easily prepare Li_2S-based cathodes seems to be highly promising for the fabrication of high specific energy Li–S batteries. However, previous cycling performance tests conducted in a wide potential window of 0.01–3.0 V *vs.* Li/Li^+ revealed a poor cycling stability of the cathodes (Fig. S3). The observed fast capacity fading and, especially, the high Coulombic efficiency (around 101–125%) are explained by the overdischarging voltage in which was exposed the facilely prepared cathode with high content of active material (2–3 mg_{Li2S} cm^{-1}). At the discharge potential of 0.01 V *vs.* Li/Li^+, various undesired side phenomena can occur—large volume expansion of the particles upon lithiation with partially damage of the formed SEI and the rapid depletion of electrolyte compounds with a continuously growth of the SEI film—which isolates the active material from the conductive current collector. In industry, the constraint of the potential window of LIBs has been commonly used for stabilizing the cathode reactions. The safe operating discharging/charging voltages are regularly delimited depending on the stable electrochemical reaction region of the battery system. It is worth mentioning that the activated cathode shows merely capacitive currents between 0.01–1.2 V *vs.* Li/Li^+ with a low capacity contribution of ≈55 mA h g^{-1} (Fig. S4), indicating that the formed Li_2S-based cathode is not electrochemically active in the applied potential window. Considering the above-mentioned aspects, the voltage cut-off was limited to 0.8 V *vs.* Li/Li^+ after the activation cycle in order to avoid side reactions and stabilize the positive electrode. Impedance analysis (Fig. S5) reveals that a deep discharge (i.e. 0.01 V *vs.* Li/Li^+) causes a notable increase of the SEI resistance during cycling triggered by a continuous growth of the SEI film, resulting in a high film resistance for lithium ions and thus lower reversibility. In contrast, the cell cycled under delimited voltage cut-off (i.e. 0.8 V *vs.* Li/Li^+) shows a lower and almost constant SEI resistance, which implies a considerably diminishing of the SEI film growing. Fig. 3c shows the discharging/charging voltage profiles corresponding to the first four cycles after activation at a C-rate of 0.1. The initial cycle displays a lower capacity in contrast to the activation cycle (970 *vs.* 2020 mA h g^{-1}, respectively). However, high capacity retention is observed in subsequent cycles, demonstrating an improved reversibility. As shown in Fig. 3d, the cyclic voltammograms recorded between 0.8–3.0 V *vs.* Li/Li^+ exhibit a good reversibility and cell stability evidenced from the almost overlapping CV curves. Notably, rather than the typical redox reaction behavior of Li–S cells, the voltage profile (Fig. 3c) and the CV curves (Fig. 3d) of our sulfur-based cathode are similar to those sulfur-polyacrylonitrile (SPAN) composite and sulfur-confined ultramicroporous carbon cathode systems, which are governed by a solid-state chemistry reaction [40–43]. This behavior would explain the lack of soluble polysulfide formation and therefore the good performance of this simple sulfur-based cathode in a carbonate-based electrolyte. Note that Mo is always present after the initial discharging process, which may modify the sulfur chemistry and thus the redox behavior of the Li/S couple [20]. The main role of the Mo is still quite controversial. For instance, Sen et al. determined the formation of metallic Mo particles by X-ray absorption spectroscopy

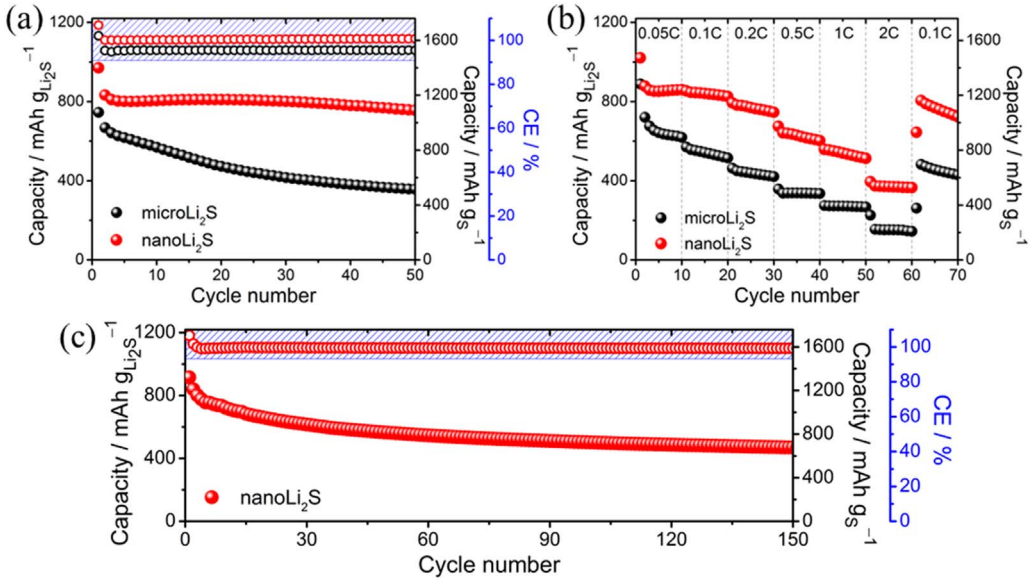

Fig. 4. (a) Comparative cycling performance at C-rate of 0.1 and (b) comparative rate performance of Li–Li_2S half-cells with microLi_2S and nanoLi_2S cathodes. (c) Long-term cycling performance at a C-rate of 0.5 for the half-cell with a nanoLi_2S-based cathode. All the cells were tested between 0.8 and 3.0 *vs.* Li/Li^+ after activation.

after the first discharge but, simultaneously, no Mo–S bonds were observed in the complete discharging/charging stage [19]. Otherwise, Doan-Nguyen et al. reported that the sulfur species in the LiPS chains is reduced and oxidized upon, respectively, discharge and charge while Mo maintains an oxidation state of (+4), which means that Mo–S bonds remain intact during cycling in a carbonate-based electrolyte [44]. Undoubtedly, further works are needed to fully understand the main interaction between Mo and sulfur-related species.

The use of nanosized Li_2S particles is expected to promote the physical confinement and buffer the sulfur volume changes during cycling [45], and thus protects the integrity of the cathode and improves the electrochemical performance of Li–S batteries. In order to prove this assumption, cathode electrodes with MoS_2 microparticles were used for control. The cyclability of the Li–S half-cells with initially nano- and microsized MoS_2 cathodes was evaluated by galvanostatic dis-/charging between 0.8 and 3.0 V *vs.* Li/Li^+ at a current rate of 0.1 C. The initial MoS_2 content in the cathodes is set to 80 wt%, corresponding to 40 wt% of Li_2S based on cathode preparation and after complete conversion of MoS_2 to Li_2S. Hereinafter, all cells were previously activated between 0.01–3.0 *vs.* Li/Li^+. As shown in Fig. 4a, the Li–S half-cell with the Li_2S cathode derived from the starting MoS_2 microparticles (denoted as microLi_2S) displays an initial discharge capacity (with the corresponding capacity based on sulfur in parentheses) of 745 mA h g^{-1} (1070 mA h g^{-1}). The cell also shows a gradual decrease of capacity reaching 358 mA h g^{-1} (514 mA h g^{-1}) and a low CE of 95.4% after 50 cycles. In contrast, the Li–S half-cell with Li_2S cathode resulting from the MoS_2 nanoparticles (denoted as nanoLi_2S) exhibits an initially high discharge capacity of 971 mA h g^{-1} (1395 mA h g^{-1}). After 50 cycles, the cell offers superior capacity retention of 756 mA h g^{-1} (1086 mA h g^{-1}) and excellent CE close to 100%. State-of-the-art Li–S batteries operated in ether-based electrolyte systems require the use of some additives (e.g. $LiNO_3$) to form a protecting layer on the lithium metal to further avoid the surface passivation of the anode by deposition of polysulfide species, and thus improve the overall cycle life and efficiency of the cells. Astonishingly, the good reversibility of our oversimplified Li_2S cathode operated in a carbonate-based electrolyte system not only reveals that it does not require any additive but, most importantly, also demonstrates the absence of the polysulfide shuttle phenomenon. This proficient confinement could be explained by the formation of a highly stable polymeric gel-like SEI layer which acts as an ultimate shield against the active material loss but also permeable to Li^+ ions [19]. The beneficial effect of the well-entrapped but still active sulfur-related species is also evidenced by the evaluation of the rate capability acquired at current rates from 0.05 C to 2 C (Fig. 4b). Additionally, a long-term cycling test of the Li–S cell with the nanosized Li_2S cathode was conducted at a C-rate of 0.5 (Fig. 4c). The Li–S cell shows an initial discharging capacity of 915 mA h g^{-1} (1314 mA h g^{-1}), good cycling stability with a high reversible capacity of 488 mA h g^{-1} (701 mA h g^{-1}) and a notable CE of 99.2% after 150 cycles.

The energy density is a critical parameter to be improved in Li–S cells by increasing the sulfur loading in order to provide competitive performances compared with high-voltage lithium ion batteries. However, the areal loading of the Li_2S and S cathodes in most reported works is lower than 2.0 mg cm^{-2}, which is insufficient to fulfill the demands for high-energy density batteries. To further demonstrate the potential of the nanosized Li_2S-based cathode for its practical implementation in Li–S batteries, the areal Li_2S loading was significantly increased to 10.7 mg_{Li2S} cm^{-2}. Fig. 5 shows the cycling performance of the Li_2S-based cathode carried out at a C-rate of 0.1. Despite the considerably high Li_2S content of the simply designed cathodes, the cells display a stable reversibility and good active material utilization. What is even more significant, the cell with 10.7 mg_{Li2S} cm^{-2} delivered an outstanding average areal capacity of 7.5 mA h cm^{-2}. This notable high areal capacity is not only one of the highest reported so far in comparison with sophisticated MoS_2- or Li_2S-based cathodes [10,46–48], but also is almost two-fold higher than that of the value of up-to-date commercial LIBs [49].

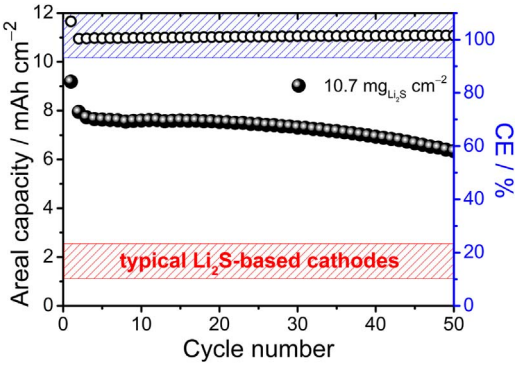

Fig. 5. Cycling performance of the Li–Li_2S half-cell with a simple-prepared Li_2S-based cathode containing an ultrahigh areal Li_2S loading of 10.7 mg cm^{-2} cycled between 0.8 and 3.0 *vs.* Li/Li^+ (after activation) and at a current rate of 0.1 C.

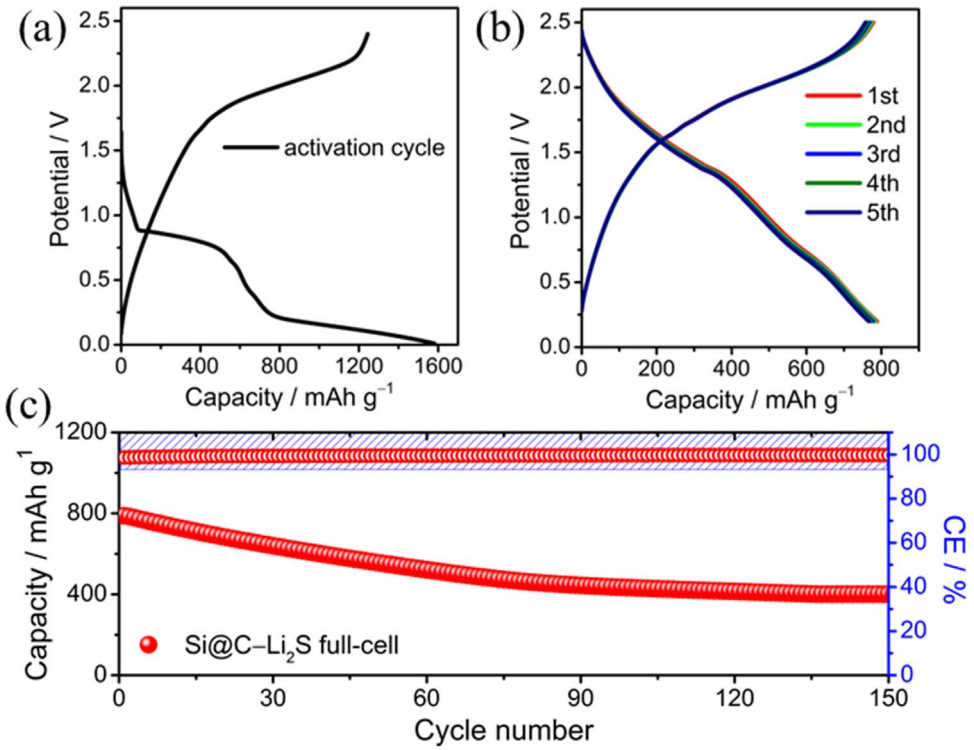

Fig. 6. (a) Galvanostatic discharging/charging curves of the activation cycle in a voltage window of 0.01–2.5 V and (b) the subsequent five cycles of the Si@C–Li_2S full-cell at a current rate of 250 mA g^{-1} and a voltage window of 0.2–2.5 V. (c) Cycling performance of the Si@C–Li_2S full-cell performed at a current rate of 250 mA g^{-1} and within a potential window of 0.2–2.5 V. Capacity based on sulfur mass.

3.3. Electrochemical performance (full-cell)

The use of metallic lithium anodes is impractically for secondary batteries due to electrolyte depletion, low reversibility, lithium dendrite formation and the associated internal short circuit, resulting in critical safety hazards [11]. Silicon is a promising anode candidate for high-energy post-LIBs due to its high specific capacity which is up to 10 times higher than commercially used graphitic anodes. Generally, silicon anodes show best performance in carbonate-based electrolytes consisting of 1 M $LiPF_6$ in EC/DMC with FEC or VC additives [24]. However, Li–S half-cells fail to operate in carbonate-based electrolyte, mostly due to side reactions—substitution reaction or nucleophilic addition—between polysulfide species and electrolyte components, resulting in an abrupt capacity fading [35]. On the other hand, Si–S full-cells cycled in ether-based electrolytes (e.g. 1,3-dioxolane/1,2-dimethoxyethane) present poor performance [50]. Therefore, high-performance Si–S full-cells in carbonate-based electrolyte have rarely been reported [51]. Considering this scenario, the coupling of our simple cathode but unexpectedly highly stable Li_2S-based cathode in a carbonate-based electrolyte with a lithiated Si anode could ensure a negligible polysulfide contamination to further improve the overall electrochemical performance of the full-cell. To provide the proof-of-concept, the initial nanoMoS_2-containing cathode was coupled with a lithiated and nanostructured silicon/carbon composite (LiSi@C) serving as negative electrode [23,24]. Details on the anode preparation are given in the experimental section. The LiSi@C anode in the main is used as the necessary lithium source. Pre-activation cycle to produce the nanosized Li_2S-based cathode was performed between 0.01 and 2.5 V at a current rate of 250 mA g^{-1}. Full-cells (Si@C *vs.* Li_2S) were tested at a current rate of 250 mA g^{-1} and within a potential window of 0.2–2.5 V. The silicon anode was roughly 20% over dimensioned in terms of capacity. The galvanostatic dis-/charging curves of the activation cycle and the subsequent five cycles of the full-cell are shown in Fig. 6a and b, respectively. The prompt irreversible conversion of MoS_2 to Li_2S and Mo together with the SEI formation is clearly proven as plateau at a potential of ≈0.1 V (Fig. 6a). However, the plateau is not fully elongated compared to the half-cell configuration (Fig. 3a) and thus MoS_2 may not fully react to Li_2S. The reason for this incomplete reaction is mainly because of the higher potential of the lithiated silicon electrode compared to the metallic lithium anode which shifts the entire reactions about 0.3 V to lower potentials. As shown in Fig. 6b, the first five dis-/charging curves after activation are well-overlapped, indicating excellent reversibility and cell stability. In general, the full-cell system presents a similar voltage plateau trend compared with the Li–Li_2S half-cells. Further galvanostatic cycling performance of the full-cell is shown in Fig. 6c. Despite the use of a so far unsophisticated sulfur-based cathode, the Si@C–Li_2S full-cell offers outstanding performance with an initial discharging capacity of 788 mA h g^{-1} along with a high reversible capacity of 410 mA h g^{-1} and degradation rate of 0.32% per cycle after 150 cycles at 250 mA g^{-1}.

On the whole, the electrochemical performance of the Li–S half-cells with an easy-to-prepare Li_2S-based cathode operated in a carbonate-based electrolyte exceeds that of typical Li–S cells in ether-based electrolyte systems, especially in terms of areal capacity. Furthermore, the remarkable stability of the cathode in carbonate-based electrolyte allows pairing it with a Si anode to build a stable (Li) Si–Li_2S full-cell with high-performance. The outstanding stability of the *in-situ* synthesized Li_2S cathode are attributed to the exceptional features of the polymeric gel-like SEI film which restrain the active material on the positive electrode for its further reutilization.

4. Conclusions

Throughout this work, we have demonstrated that controlling the MoS_2 chemistry it is possible to obtain nanosized Li_2S (≈15 nm) *via* full lithiation and irreversible electrochemical decomposition of MoS_2 nanoparticles at low potential (i.e. 0.01 V *vs.* Li/Li^+). Also we showed the high importance of using MoS_2 nanoparticles instead of MoS_2 microparticles as starting material for Li_2S formation, and its critical effect on the final cell performance. Notably, the obtained Mo/Li_2S-based cathode do not form

soluble polysulfide intermediates, allowing its operation in carbonate-based electrolytes by limiting the potential window of the cells to 0.8–3.0 V. The viable and facilely designed Mo/Li_2S-based cathode showed a remarkable improvement of the cycle stability, delivering high average capacities of 756 and 1086 mA h g^{-1} based on Li_2S and sulfur mass, respectively. Moreover, the Li–S cell with an ultrahigh Li_2S loading of 10.7 mg cm^{-2} delivered a high average areal capacity of 7.5 mA h cm^{-2}, which is 3–6 times higher than that of typical MoS_2- or Li_2S-based cathodes. The absence of electrolyte-dissoluble polysulfides due to our sulfur-based cathode, carbonate-based electrolytes can be used skipping the negative issues of ether-based electrolytes, especially in combination of our cathode with (Li)Si anodes when assembling a full-cell system. As a result of the stable cathode, the Si@C–Li_2S full-cell exhibited a good cycling performance with high initial discharge capacity of 788 mA h g_S^{-1}, reversible capacity of 410 mA h g_S^{-1} and low capacity degradation of 0.32% per cycle, after 150 cycles at 250 mA g^{-1}. We believe this straightforward strategy for the preparation of highly load Li_2S cathodes will encourage further research works in the topic and has great potential for practical applications in high energy density sulfur-based battery technology.

Author contributions

The manuscript was written through contributions of all authors. All authors have given approval to the final version of the manuscript.

Conflict of interest

The authors declare no competing financial interest.

Acknowledgment

The authors thank A. Voß, A. Voidel and R. Buckan for their valuable technical support. Dr. Ralf Hauser from the Fraunhofer IFAM is gratefully acknowledged for providing the copper foam. We also thank Dr. Jürgen Thomas for ELDISCA programming. This work was support by the German Federal Ministry of Education and Research (BMBF) through the Excellent Battery – WING center "Batteries - Mobility in Saxony" (grant number 03X4637C).

Appendix A. Supplementary material

Supplementary data associated with this article can be found in the online version at doi:10.1016/j.ensm.2017.03.013.

References

[1] B. Dunn, H. Kamath, J.-M. Tarascon, Science 334 (2011) 928–935.
[2] V. Etacheri, R. Marom, R. Elazari, G. Salitra, D. Aurbach, Energy Environ. Sci. 4 (2011) 3243–3262.
[3] Z.W. Seh, Y. Sun, Q. Zhang, Y. Cui, Chem. Soc. Rev. 45 (2016) 5605–5634.
[4] Oxis energy, Technology – Oxis Energy, 2017 [online]. Available at: ⟨http://oxisenergy.com/technology/⟩ (Accessed 6 January 2017).
[5] X. Ji, K.T. Lee, L.F. Nazar, Nat. Mater. 8 (2009) 500–506.
[6] N. Jayaprakash, J. Shen, S.S. Moganty, A. Corona, L.A. Archer, Angew. Chem. Int. Ed. 50 (2011) 5904–5908.
[7] G. He, S. Evers, X. Liang, M. Cuisinier, A. Garsuch, L.F. Nazar, ACS Nano 7 (2013) 10920–10930.
[8] Z. Wei Seh, W. Li, J.J. Cha, G. Zheng, Y. Yang, M.T. McDowell, P.-C. Hsu, Y. Cui, Nat. Commun. 4 (2013) 1331.
[9] Z.W. Seh, H. Wang, P.-C. Hsu, Q. Zhang, W. Li, G. Zheng, H. Yao, Y. Cui, Energy Environ. Sci. 7 (2014) 672–676.
[10] M. Kohl, J. Brückner, I. Bauer, H. Althues, S. Kaskel, J. Mater. Chem. A 3 (2015) 16307–16312.
[11] C. Barchasz, F. Molton, C. Duboc, J.-C. Leprêtre, S. Patoux, F. Alloin, Anal. Chem. 84 (2012) 3973–3980.
[12] Y.-S. Su, A. Manthiram, Nat. Commun. 3 (2012) 1166.
[13] S.-H. Chung, A. Manthiram, Adv. Funct. Mater. 24 (2014) 5299–5306.
[14] J. Balach, T. Jaumann, M. Klose, S. Oswald, J. Eckert, L. Giebeler, J. Phys. Chem. C 119 (2015) 4580–4587.
[15] J. Balach, H.K. Singh, S. Gomoll, T. Jaumann, M. Klose, S. Oswald, M. Richter, J. Eckert, L. Giebeler, ACS Appl. Mater. Interfaces 8 (2016) 14586–14595.
[16] L. Suo, Y.-S. Hu, H. Li, M. Armand, L. Chen, Nat. Commun. 4 (2013) 1481.
[17] L. Ma, H. Zhuang, Y. Lu, S.S. Moganty, R.G. Hennig, L.A. Archer, Adv. Energy Mater. 4 (2014) 1400390.
[18] T. Stephenson, Z. Li, B. Olsen, D. Mitlin, Energy Environ. Sci. 7 (2014) 209–231.
[19] U.K. Sen, P. Johari, S. Basu, C. Nayak, S. Mitra, Nanoscale 6 (2014) 10243–10254.
[20] J. Xiao, X. Wang, X.-Q. Yang, S. Xun, G. Liu, P.K. Koech, J. Liu, J.P. Lemmon, Adv. Funct. Mater. 21 (2011) 2840–2846.
[21] X. Fang, C. Hua, X. Guo, Y. Hu, Z. Wang, X. Gao, F. Wu, J. Wang, L. Chen, Electrochim. Acta 81 (2012) 155–160.
[22] X. Fang, X. Guo, Y. Mao, C. Hua, L. Shen, Y. Hu, Z. Wang, F. Wu, L. Chen, Chem. Asian J. 7 (2012) 1013–1017.
[23] T. Jaumann, J. Balach, M. Klose, S. Oswald, U. Langklotz, A. Michaelis, J. Eckert, L. Giebeler, Phys. Chem. Chem. Phys. 17 (2015) 24956–24967.
[24] T. Jaumann, J. Balach, U. Langklotz, V. Sauchuk, M. Fritsch, A. Michaelis, V. Teltevskij, D. Mikhailova, S. Oswald, M. Klose, G. Stephani, R. Hauser, J. Eckert, L. Giebeler, Energy Storage Mater. 6 (2017) 26–35.
[25] J. Thomas, T. Gemming, in: Proceedings of the 14th European Microscopy Congress, Aachen Germany, Springer, 2008, pp. 231–232.
[26] L. Lutterotti, D. Chateigner, S. Ferrari, J. Ricote, Thin Solid Films 450 (2004) 34–41.
[27] R.G. Dickinson, L. Pauling, J. Am. Chem. Soc. 45 (1923) 1466–1471.
[28] V. Petkov, S. Billinge, P. Larson, S. Mahanti, T. Vogt, K. Rangan, M. Kanatzidis, Phys. Rev. B 65 (2002) 092105.
[29] E. Zintl, A. Harder, B. Dauth, Z. Elektrochem. 40 (1934) 588–593.
[30] S.K. Das, R. Mallavajula, N. Jayaprakash, L.A. Archer, J. Mater. Chem. 22 (2012) 12988–12992.
[31] K. Xu, Chem. Rev. 114 (2014) 11503–11618.
[32] J. Chen, Q. Zhang, M. Zeng, N. Ding, Z. Li, S. Zhong, T. Zhang, S. Wang, G. Yang, J. Solid State Electrochem. 20 (2016) 1285–1294.
[33] Y. Gong, S. Yang, L. Zhan, L. Ma, R. Vajtai, P.M. Ajayan, Adv. Funct. Mater. 24 (2014) 125–130.
[34] D. Xie, W. Tang, X. Xia, D. Wang, D. Zhou, F. Shi, X. Wang, C. Gu, J. Tu, J. Power Sources 296 (2015) 392–399.
[35] T. Yim, M.-S. Park, J.-S. Yu, K.J. Kim, K.Y. Im, J.-H. Kim, G. Jeong, Y.N. Jo, S.-G. Woo, K.S. Kang, Electrochim. Acta 107 (2013) 454–460.
[36] D. Pan, S. Wang, B. Zhao, M. Wu, H. Zhang, Y. Wang, Z. Jiao, Chem. Mater. 21 (2009) 3136–3142.
[37] Y. Mao, H. Duan, B. Xu, L. Zhang, Y. Hu, C. Zhao, Z. Wang, L. Chen, Y. Yang, Energy Environ. Sci. 5 (2012) 7950–7955.
[38] J. Balach, H. Wu, F. Polzer, H. Kirmse, Q. Zhao, Z. Wei, J. Yuan, RSC Adv. 3 (2013) 7979–7986.
[39] R. Song, H. Song, J. Zhou, X. Chen, B. Wu, H.Y. Yang, J. Mater. Chem. 22 (2012) 12369–12374.
[40] J. Wang, J. Yang, C. Wan, K. Du, J. Xie, N. Xu, Adv. Funct. Mater. 13 (2003) 487–492.
[41] S. Wei, L. Ma, K.E. Hendrickson, Z. Tu, L.A. Archer, J. Am. Chem. Soc. 137 (2015) 12143–12152.
[42] M. Helen, M.A. Reddy, T. Diemant, U. Golla-Schindler, R.J. Behm, U. Kaiser, M. Fichtner, Sci. Rep. 5 (2015) 12146.
[43] S. Xin, L. Gu, N.-H. Zhao, Y.-X. Yin, L.-J. Zhou, Y.-G. Guo, L.-J. Wan, J. Am. Chem. Soc. 134 (2012) 18510–18513.
[44] V.V.T. Doan-Nguyen, K.S. Subrahmanyam, M.M. Butala, J.A. Gerbec, S.M. Islam, K.N. Kanipe, C.E. Wilson, M. Balasubramanian, K.M. Wiaderek, O.J. Borkiewicz, K.W. Chapman, P.J. Chupas, M. Moskovits, B.S. Dunn, M.G. Kanatzidis, R. Seshadri, Chem. Mater. 28 (2016) 8357–8365.
[45] M. Wu, Y. Cui, Y. Fu, ACS Appl. Mater. Interfaces 7 (2015) 21479–21486.
[46] L. Qie, A. Manthiram, Chem. Commun. 52 (2016) 10964–10967.
[47] Z.W. Seh, J.H. Yu, W. Li, P.-C. Hsu, H. Wang, Y. Sun, H. Yao, Q. Zhang, Y. Cui, Nat. Commun. 5 (2014) 5017.
[48] Z. Xu, X. Shen, Q. Zhang, J. Li, L. Kong, L. Cao, J. Huang, Part. Part. Syst. Charact. 33 (2016) 311–315.
[49] J. Song, T. Xu, M.L. Gordin, P. Zhu, D. Lv, Y.-B. Jiang, Y. Chen, Y. Duan, D. Wang, Adv. Funct. Mater. 24 (2014) 1243–1250.
[50] T. Jaumann, J. Balach, M. Klose, S. Oswald, J. Eckert, L. Giebeler, J. Electrochem. Soc. 163 (2016) A557–A564.
[51] R. Cao, W. Xu, D. Lv, J. Xiao, J.-G. Zhang, Adv. Energy Mater. 5 (2015) 1402273.